Article

FSTL-1 loaded 3D bioprinted vascular patch regenerates the ischemic heart tissue

Biomanufacturing a 3D vascular FSTL1-laden cardiac patch

Boeun Hwang, Lauren Korsnick, Ming Shen, ..., Mostafa Abdalla, Holly Bauser-Heaton, Vahid Serpooshan

vahid.serpooshan@bme.gatech.edu

Highlights
A vascular cardiac patch is biofabricated through mold-casting and 3D bioprinting

The patch has tissue-like stiffness and microstructure, with perfusable vasculature

FSTL1 in patch reduces fibrosis and enhances vascularization and CM proliferation

FSTL1-patch diminishes adverse cardiac remodeling post myocardial infarction

iScience

Article

FSTL-1 loaded 3D bioprinted vascular patch regenerates the ischemic heart tissue

Boeun Hwang,[1] Lauren Korsnick,[1] Ming Shen,[2] Linqi Jin,[1] Yamini Singh,[1] Mostafa Abdalla,[1] Holly Bauser-Heaton,[1,2,3,4] and Vahid Serpooshan[1,2,3,5,*]

SUMMARY

Cardiac patch strategies are developed as a promising approach to regenerate the injured heart after myocardial infarction (MI). This study integrated 3D bioprinting and cardioprotective paracrine signaling to fabricate vascular patch devices containing endothelial cells (ECs) and the regenerative follistatin-like 1 (FSTL1) peptide. Engineered patch supported the 3D culture of ECs in both static and dynamic culture, forming a uniform endothelium on the printed channels. Implantation of vascular patch onto a rat model of acute MI resulted in significant reduction of scar formation, left ventricle dilation, and wall thinning, as well as enhanced ejection fraction. Furthermore, increased vascularization and proliferation of cardiomyocytes were observed in hearts treated with patches. These findings highlight the remarkable capacity of 3D bioprinted vascular patch to augment the endogenous regenerative capacity of mammalian heart, together with the exogenous cardioprotective function, to serve as a robust therapeutic device to treat acute MI.

INTRODUCTION

Myocardial infarction (MI) is an ischemic heart injury caused by the blocking of coronary arteries. The insufficient blood supply to the myocardium results in irreversible damage to the heart muscle and impairs heart function. Despite the recent advances in cardiovascular research, the recovery of cardiac function and structure after MI has remained a challenge. The major difficulties with treating injured heart muscle stem from the extremely low proliferative capacity of cardiomyocytes (CMs). Since adult mammalian CMs do not effectively replicate, the damaged myocardium cannot be replaced with new healthy muscle tissue to restore cardiac function. Over the past decades, many studies have investigated novel therapies to regenerate myocardial tissue after injury.[1–3] Cardiac patches are developed as a tissue engineered device and have shown promising outcomes in restoring the cardiac structure and function after infarction.[4–7] Previous studies have demonstrated that the placement of a cardiac patch can provide mechanical support to the left ventricle (LV) and mitigate adverse remodeling.[8–10] However, the conventional patch devices have faced various challenges such as the poor capacity to regenerate myocardium and integrate with the host tissue.[11] Recent research endeavors, therefore, have explored a variety of novel approaches to further enhance the regenerative capacity and function of patch devices.[4,12–14]

Vascularization of engineered tissue analogues is essential to develop patch devices at anatomically relevant scales. Incorporating vasculature can enhance the diffusion of oxygen and nutrient throughout the cellularized scaffold, resulting in increased viability and functionality of embedded cells.[15–17] Moreover, the vascular network, pre-formed within the engineered construct, can facilitate integration with the host tissue.[18–22] Efforts have been made to create vascularized tissues by embedding endothelial cells (ECs) or microvessel fragments within the constructs.[23–27] When encapsulated inside, ECs can form self-assembled connections and create microvascular networks.[28,29] Another approach of vascularizing engineered tissues is based on creating interconnected patent channels within the 3D scaffolds during the biofabrication process.[24,30] While these strategies have resulted in significant improvement in vascularization of 3D tissues, the efficacy of forming functional vascular systems would be limited without directing proper flow through these constructs. Therefore, further research and technical advancements are focused on fabricating pre-formed 3D vascular tissue constructs that allow for long-term vascular perfusion to ensure adequate functionality and biomimicry.[31–33]

Follistatin-like 1 (FSTL1) is a glycoprotein involved in various biological processes, including cell proliferation, survival, and angiogenesis.[34–36] Its cardioprotective and angiogenic role has been highlighted in preventing adverse effects of ischemic heart injuries.[37,38] Previous studies have found that delivery or over-expression of FSTL1 in heart can significantly improve cardiac function after MI and promote regeneration of the adult myocardium.[5,39,40] While FSTL1-laden patches have been developed to leverage the cardioprotective and

[1]Wallace H. Coulter Department of Biomedical Engineering, Emory University School of Medicine and Georgia Institute of Technology, Atlanta, GA, USA
[2]Department of Pediatrics, Emory University School of Medicine, Atlanta, GA, USA
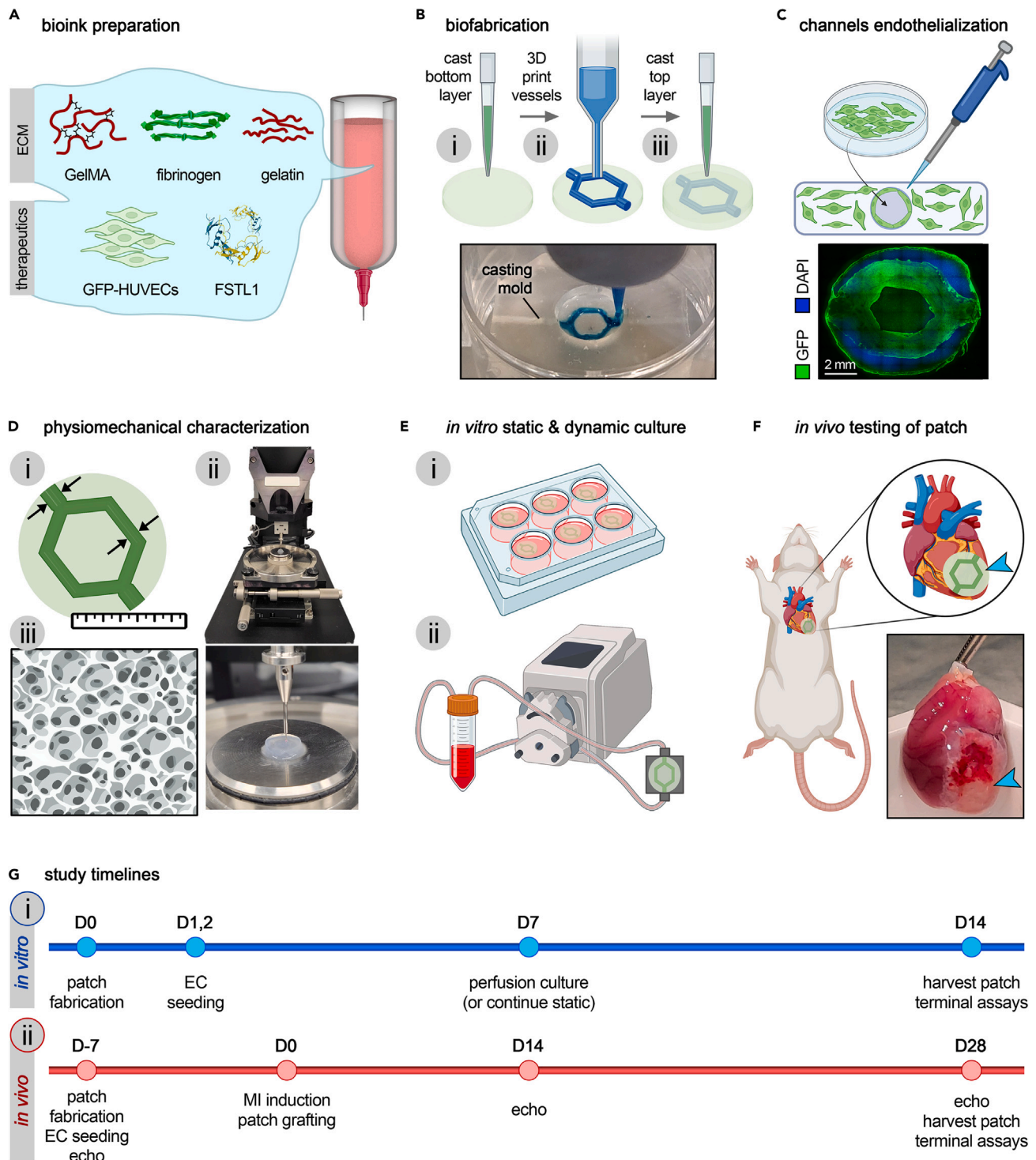[3]Children's Healthcare of Atlanta, Atlanta, GA, USA
[4]Sibley Heart Center at Children's Healthcare of Atlanta, Atlanta, GA, USA
[5]Lead contact
*Correspondence: vahid.serpooshan@bme.gatech.edu
https://doi.org/10.1016/j.isci.2024.110770

Figure 1. Schematic illustration of the research workflow

(A) A hybrid bioink formulation was developed, containing gelatin methacrylate (GelMA), fibrinogen, and sacrificial gelatin, as the three ECM components, as well as therapeutic factors, including GFP-labeled human umbilical vein endothelial cells (HUVECs) and follistatin-like 1 (FSTL1) protein.

(B) A multistep biofabrication process was developed and employed to create the 3D vascular cardiac patch. The steps included casting the bottom layer into a disc-shaped mold (i), 3D bioprinting the vascular channels via sacrificial Pluronic (ii), and casting the top layer (iii) to complete the fabrication process. The inset in the bottom shows the printing step for creating a 3D vascular network onto the bottom hydrogel layer.

(C) Fabricated patch constructs were next seeded with GFP-HUVECs, in the luminal space, to ensure full endothelialization of vascular channels. Scale bar: 2mm.

![CellPress OPEN ACCESS logo]

Figure 1. Continued

(D) Patch constructs were characterized via structural fidelity analysis (i), microindentation (ii), and scanning electron microscopy (SEM) (iii).

(E) Cellular patch constructs were tested *in vitro*, under static (i) and dynamic (ii) culture conditions using a perfusion bioreactor system.

(F) The optimal patch constructs were tested *in vivo*, in a rat model of myocardial infarction (MI), where the engineered patch was immediately grafted onto the epicardium. The arrows point to the MI/patch regions.

(G) The timelines used for the *in vitro* (i) and *in vivo* (ii) studies.

pro-proliferative effects of FSTL1, they were cast using extracellular matrix (ECM) proteins (e.g., collagen type I), lacking a functional vasculature.[5,6,41] In another report, a bi-layer proteinaceous hydrogel patch loaded with FSTL1 was 3D bioprinted and their ability to form architecturally intricate designs was demonstrated.[39] However, prior therapies were only comprised of FSTL1 and biomaterials without cellular components, which could limit the engraftment and integration of the implant with the host myocardium.[39,42] Therefore, there is evident need for studies focusing on the orchestration of bioactive materials, regenerative molecules, and cellularization of cardiac patch devices.

In this study, a 3D bioprinted perfusable vascular cardiac patch was developed and loaded with human umbilical vein ECs (HUVECs) and FSTL1 to enhance the regenerative function of the patch. The printed channel network in the patch was endothelialized to create a vessel-like structure. Engineered patches showed patent vasculature with EC lining following perfusion. In the *in vivo* assays, FSTL1-loaded endothelialized patches significantly improved the cardiac function after MI, demonstrating the promising therapeutic potential of the cellular FSTL1 patch in regenerating the adult mammalian myocardium after injury.

RESULTS

3D bioprinting of cardiac patches and their characterization

To create cardiac patch devices, a hybrid bioink was formulated at 6% GelMA, 5% gelatin, and 1% fibrinogen and loaded with GFP-HUVECs at 10M cells/mL and FSTL1 at 5 μg/mL (Figure 1A). This cellular bioink was cast into a negative mold of the patch design. A bifurcated vascular channel was extrusion-printed with a sacrificial bioink (Pluronic) and another cellular bioink layer was cast to complete the cardiac patch fabrication (Figure 1B). The patch constructs were crosslinked with UV and transferred to EC media with thrombin to polymerize fibrinogen to fibrin. Vascular channels within scaffolds were further seeded with HUVECs (in addition to bulk EC in the ink) to ensure full endothelization of lumens (Figure 1C). A series of physiomechanical characterizations were conducted to achieve optimal patch fabrication parameters (Figure 1D), followed by *in vitro* (Figure 1E) and *in vivo* (Figure 1F) assessment of cellular patch function over 2 and 4 weeks (Figure 1G).

Cardiac patches were first characterized for manufacturing fidelity and structural stability (Figure 2A). To assess the effect of encapsulating cells in the bioink in manufacturing fidelity and alterations in patch dimensions over time, both cellular and acellular patches were investigated. Fidelity ratio was calculated by comparing the measured geometric parameters to the corresponding values in the CAD (STL) model (Figure 2A, i). Therefore, a ratio value of 1 would indicate an ideal manufacturing fidelity. At the day 0 of fabrication, both cellular and acellular constructs showed fidelity ratios approaching 1.00 for the patch diameter (0.87–0.97) and channel sizes (1.10–1.16) (Figure 2A, ii-iv). However, the changes in patch dimensions after 14 days of culture at 37°C varied across the groups. The diameters of both cellular and acellular scaffolds remained consistent, with marginal increase in acellular patch diameter and decrease in cellular patch diameter (Figure 2A, ii-iv). On the other hand, the inner channel diameters of acellular patches decreased significantly for both channels 1 and 2 (Figure 2A, iv). There was a decrease in channel 1 for cellular patches that were cultured in static, but not in perfusion culture. Unlike acellular constructs, the cellular patches remained more stable during culture in both diameter and channel size.

The microindentation tests also demonstrated distinct mechanical properties of cellular versus acellular constructs on day 0. While the same composition of bioink (6% GelMA, 5% gelatin, 1% fibrinogen) was used, the addition of cells led to a decrease in patch stiffness (8.1 ± 1.2 kPa) when compared with acellular scaffolds (17.5 ± 1.7 kPa) (Figure 2B). Of note, the stiffness of cellular and acellular structures followed opposite directions after 14 days of culture. The acellular patches decreased in elastic modulus while the cellular patches showed increased moduli (Figure 2B).

Following fidelity and micro-mechanical analyses, the ultrastructure of (acellular) cardiac patches was examined using SEM (Figure 2C). Patch constructs showed a highly porous structure throughout the scaffold, with the average pore diameter of 58.2 ± 33.5 μm (Figure 2C, iv). The pore diameters ranged widely from 12.7 to 157.0 μm, and the majority of the pores had a diameter at the 25–90 μm interval.

Endothelialization and *in vitro* culture of FSTL1-loaded cardiac patches

Following fabrication of patch constructs using the composite cellular bioink with or without FSTL1, the cardiac patches were crosslinked under UV and then polymerized with thrombin (to crosslink the fibrinogen component in the ink into fibrin). The channels within the patch were hollowed out by dissolving the sacrificial Pluronic network. Subsequently, the pre-formed vasculature was seeded with HUVECs (8M cells/mL) through manual injecting of the cell suspension into the luminal space. EC seeding was performed twice, on days 1 and 2 (Figure 1G), with a 180-degree rotation of patches, to ensure uniform endothelialization of the channels. AlamarBlue reduction assay was used as measure of cell viability and growth at days 3, 7, and 14 of culture. The AlamarBlue reduction for both (−) FSTL1 and (+) FSTL1 groups significantly increased from day 3 (11.6 ± 0.8% and 12.6 ± 0.6%, respectively) to day 7 (17.8 ± 0.5% and 18.7 ± 0.7%, respectively) and reached a plateau by day 14 (16.7 ± 0.2% and 16.6 ± 1.0%, respectively) (Figure 3A).

Following the endothelialization of patches in static culture, we assessed perfusion capability of constructs (Figures 3B and 3C). Cardiac patches were endothelialized and cultured in static condition for 7 days and subsequently perfused for 7 days. IHC images of patches on day
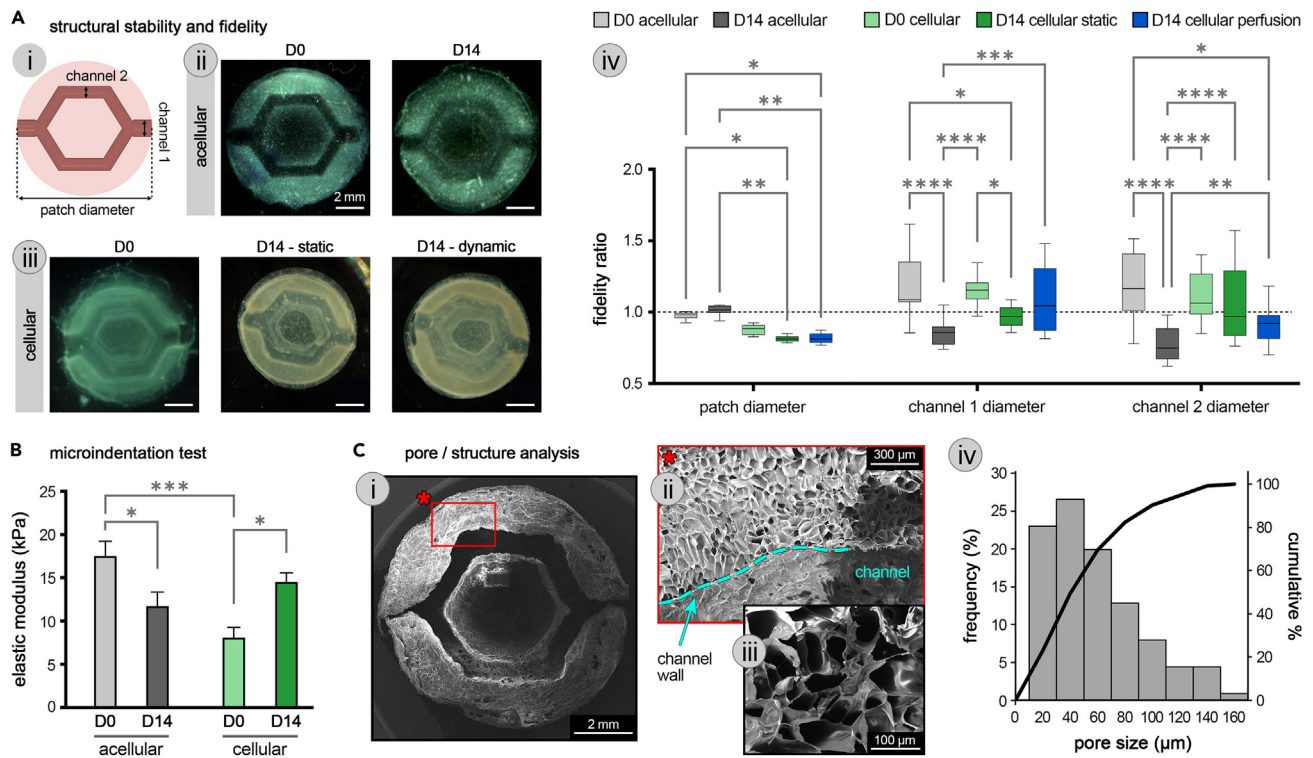
Figure 2. Characterization of biofabricated vascular patches

(A) Structural fidelity and stability were assessed by measuring various geometric parameters of the patch design (i). Bright field images of acellular (ii) and cellular (iii) patches were captured at days 0 (baseline) and 14 of culture (static and dynamic) and used to quantify the patch diameter and channels 1–2 diameter values as fidelity ratio (divided by the design values) (iv). Scale bars in all patch photos represent 2 mm. A sample size of n = 5 per group was used for fidelity calculations. Statistical significance was determined by one-way ANOVA.

(B) Micromechanical testing was performed via microindentation and elastic moduli of cardiac patches at day 0 and day 14 of culture (static) were measured. A sample size of n = 4 per group was used for mechanical tests. Data were analyzed using two-way ANOVA.
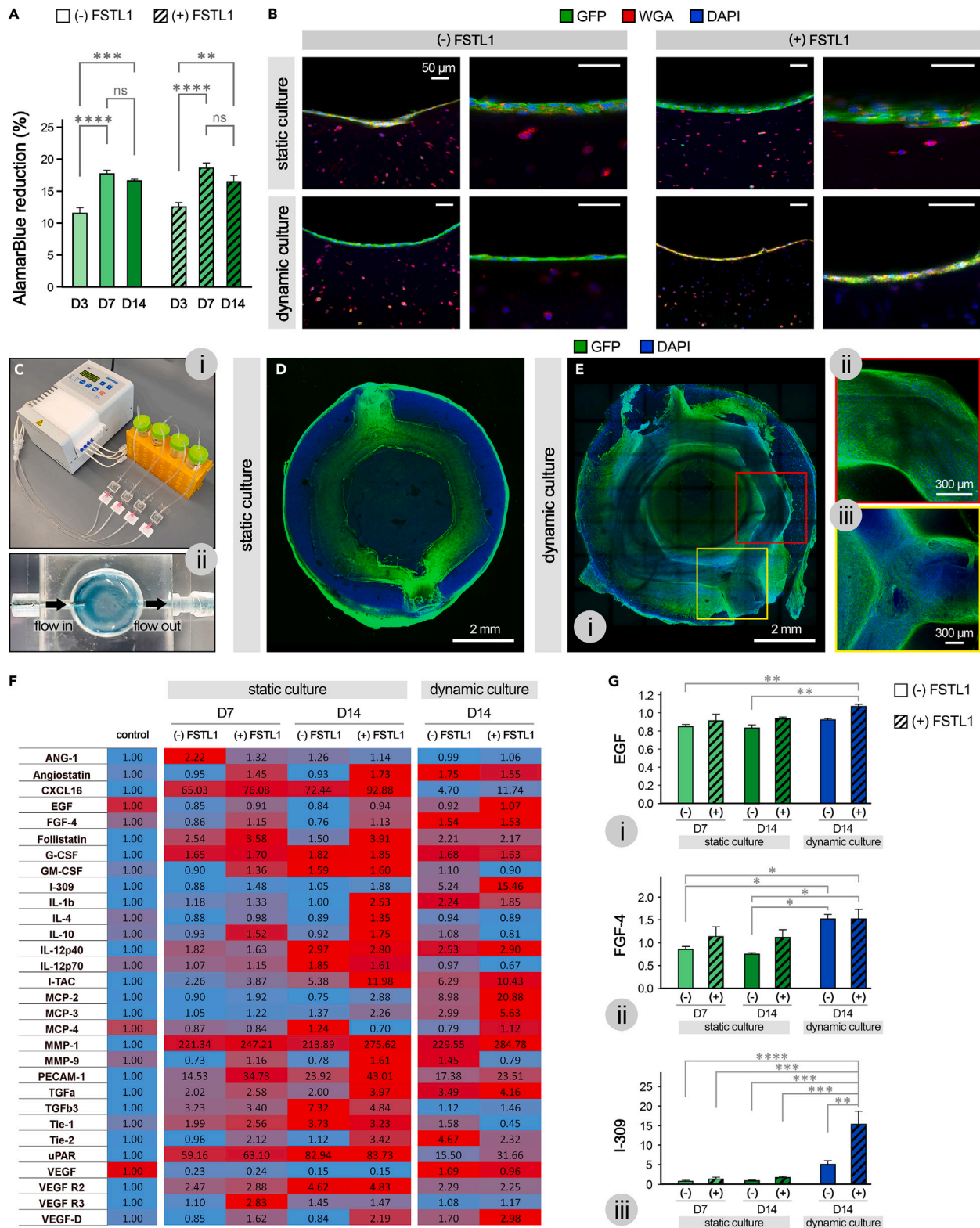
(C) Scanning electron microscopy (SEM) images (i-iii) were used to quantify pore size distribution (iv) within the 3D scaffolds. A sample size of n = 7 was used for pore size analysis. Scale bars in i, ii, and iii are 2 mm, 300 μm, and 100 μm, respectively. *: $p < 0.05$, **: $p < 0.01$, ***: $p < 0.005$, and ****: $p < 0.001$. Data represent mean ± SEM.

14 of static and dynamic culture exhibited strong expression of GFP, WGA, and DAPI of embedded and seeded HUVECs (Figure 3B). The lumen of vascular channels was uniformly covered with ECs in patches with and without FSTL1, in static and dynamic flow, mimicking the native vasculature. Moreover, IHC analysis demonstrated that HUVECs remained attached to the lumen in perfused channels and formed a thinner, single-cell layer of endothelium, compared to the multilayer EC structure in the static group (Figure 3B, top vs. bottom). Whole-mount imaging of stained constructs showed the longitudinal view of the entire vascular patches cultured in static and perfusion conditions, further confirming the full endothelialization (Figures 3D and 3E). In these images, the GFP signal was stronger within the channels of the static-cultured patch, likely due to the multilayer structure of ECs in that group.

To assess the angiogenic effect of FSTL1-loaded patch, the media supernatants were collected and tested for the levels of angiogenic factors using a multiplex ELISA panel. Culturing of endothelialized cardiac patches led to increase in the majority of angiogenic factors compared to the baseline control with unconditioned culture media (Figure 3F). FSTL1-loaded patches induced higher levels of angiogenic activities compared to the patches without FSTL1. Significantly higher levels of EGF, FGF-4, and I-309 were detected in the FSTL1-loaded patches, cultured under perfusion (Figure 3G, i-iii). Of note, the static culture groups did not show significant differences in the angiogenic factor levels in the (−) and (+) FSTL1 conditions.

In vivo implantation and therapeutic effect of FSTL1-loaded cardiac patch

Therapeutic capability of the 3D biofabricated vascular patches was evaluated in a rat model of MI (Figure 4A, i-iv). Masson's trichrome staining of the harvested hearts showed that after 4 weeks of implantation, patches remained adherent to the host myocardium and maintained an effective interface with the recipient tissue (Figures 4B and 4C). The MI group exhibited the most severe level of adverse ventricular remodeling, including the LV dilation, wall thinning, and fibrosis, as opposed to the patch treated groups (Figures 4B–4D). The epicardial application of patch + FSTL1 significantly decreased the fibrotic area within the LV from 30.8 ± 4.5% to 16.9 ± 3.5% ($p < 0.05$; Figure 4D). Longitudinal echocardiography was performed over the 4-week study period. The long-axis and short-axis images showed that implantation of cardiac

F		static culture				dynamic culture	
		D7		D14		D14	
	control	(-) FSTL1	(+) FSTL1	(-) FSTL1	(+) FSTL1	(-) FSTL1	(+) FSTL1
ANG-1	1.00	2.22	1.32	1.26	1.14	0.99	1.06
Angiostatin	1.00	0.95	1.45	0.93	1.73	1.75	1.55
CXCL16	1.00	65.03	76.08	72.44	92.88	4.70	11.74
EGF	1.00	0.85	0.91	0.84	0.94	0.92	1.07
FGF-4	1.00	0.86	1.15	0.76	1.13	1.54	1.53
Follistatin	1.00	2.54	3.58	1.50	3.91	2.21	2.17
G-CSF	1.00	1.65	1.70	1.82	1.85	1.68	1.63
GM-CSF	1.00	0.90	1.36	1.59	1.60	1.10	0.90
I-309	1.00	0.88	1.48	1.05	1.88	5.24	15.46
IL-1b	1.00	1.18	1.33	1.00	2.53	2.24	1.85
IL-4	1.00	0.88	0.98	0.89	1.35	0.94	0.89
IL-10	1.00	0.93	1.52	0.92	1.75	1.08	0.81
IL-12p40	1.00	1.82	1.63	2.97	2.80	2.53	2.90
IL-12p70	1.00	1.07	1.15	1.85	1.61	0.97	0.67
I-TAC	1.00	2.26	3.87	5.38	11.98	6.29	10.43
MCP-2	1.00	0.90	1.92	0.75	2.88	8.98	20.88
MCP-3	1.00	1.05	1.22	1.37	2.26	2.99	5.63
MCP-4	1.00	0.87	0.84	1.24	0.70	0.79	1.12
MMP-1	1.00	221.34	247.21	213.89	275.62	229.55	284.78
MMP-9	1.00	0.73	1.16	0.78	1.61	1.45	0.79
PECAM-1	1.00	14.53	34.73	23.92	43.01	17.38	23.51
TGFa	1.00	2.02	2.58	2.00	3.97	3.49	4.16
TGFb3	1.00	3.23	3.40	7.32	4.84	1.12	1.46
Tie-1	1.00	1.99	2.56	3.73	3.23	1.58	0.45
Tie-2	1.00	0.96	2.12	1.12	3.42	4.67	2.32
uPAR	1.00	59.16	63.10	82.94	83.73	15.50	31.66
VEGF	1.00	0.23	0.24	0.15	0.15	1.09	0.96
VEGF R2	1.00	2.47	2.88	4.62	4.83	2.29	2.25
VEGF R3	1.00	1.10	2.83	1.45	1.47	1.08	1.17
VEGF-D	1.00	0.85	1.62	0.84	2.19	1.70	2.98

Figure 3. *In vitro* culture of vascular endothelialized patches with and without FSTL1

(A) AlamarBlue reduction as a measure of metabolic activity of human umbilical vein endothelial cells (HUVECs) within the 3D patches in static culture, with and without FSTL1 (n = 4 per group) in the constructs, at days 3, 7, and 14. Data were assessed using one-way ANOVA.

Figure 3. Continued

(B) Immunohistochemical (IHC) imaging of endothelialized vascular channels in the patches after 14 days of static (top) and dynamic (bottom) culture, in the presence or absence of FSTL1 in the constructs. Green, red, and blue colors represent GFP (HUVECs), WGA (plasma membrane), and DAPI (nuclei) staining. For each condition, images at two magnifications are presented. Scale bars in all images show 50 μm.

(C) i-ii: experimental set-up used for perfusion (dynamic culture) of cellular cardiac patches.

(D and E) Whole-mount IHC imaging of fully endothelialized patches after 14 days of static (D) and dynamic (E, i-iii) culture. Red and yellow boxes in (E, ii-iii) show magnified views of the regions highlighted in (i). Scale bars in D and E (i) are 2 mm, and ones in E (ii) and E (iii) are 300 μm.

(F) A heatmap of angiogenesis markers for different study groups at days 7–14 of culture. A kit containing a microarray of various conjugated antibodies was used to test supernatant samples. Fresh culture media samples were used as control for normalization (n = 3 per group).

(G) i-iii: quantitative analysis of selected angiogenic factors (from the heatmap in F), showing some of the most significant differences across study groups (n = 3 per group). Data analyzed with two-way ANOVA. *: $p < 0.05$, **: $p < 0.01$, ***: $p < 0.005$, and ****: $p < 0.001$. Data represent mean ± SEM.

patches can improve cardiac function and reduce LV remodeling after MI (Figure 4E). At week 4 after the MI, the group treated with patch + FSTL1 exhibited significantly higher EF (55.9 ± 3.4%) compared to the MI-only group (41.6 ± 3.9%, $p < 0.05$; Figure 4F, i). Both patch and patch + FSTL1 groups showed higher levels of EF compared to the MI-only group in both weeks 2 and 4, indicating the epicardial patch delivery could (partly) protect/restore the heart function post injury. In addition, the patch treated groups demonstrated reduced LV wall thinning compared to the MI-only group where the LV wall thickness continued to decrease over 4 weeks (Figure 4F, ii). Based on the histology measurements, there was also diminished LV dilation at week 4 in the patch treated groups (patch only at 5.6 ± 0.3 mm and patch + FSTL1 at 5.4 ± 0.2 mm) compared to the MI-only group (6.3 ± 0.3 mm) (Figures 4F and iii).

In addition to the functional assessment, IHC analysis of the harvested heart tissues confirmed the cardioprotective effect of FSTL1-loaded cardiac patches (Figure 5). Confocal images revealed that by week 4, implanted patches effectively integrated with the host myocardium (Figure 5A). Further, the MI + patch + FSTL1 group showed more expression of vWF positive areas within the injury sites among all groups (Figures 5B and 5C). To understand the regional differences in neovascularization in response to the patch treatment, the border and infarct zones (BZ and IZ, respectively) were stained with cardiac troponin (cTnT) and vWF (Figure 5B). There was insignificant difference ($p > 0.05$) in the vessel area % in the border zone of MI-only and MI + patch treated groups (Figure 5C). In contrast, MI + patch + FSTL1 treated group showed substantial ($p < 0.05$) increase in the vessel area in the infarct zone, compared to both the MI-only and MI + patch groups (Figure 5C, bottom).

To further understand the regenerative potential of FSTL1-loaded cardiac patch on the ischemic myocardium, the proportion of CMs that express proliferative marker Ki67 was examined at week 4 (Figures 5D and 5E). IHC images and quantification of the signal indicated that the patch + FSTL1 treated hearts showed the highest percentage of CM proliferation (Ki67+ cells as evidence of DNA synthesis[43]). While the % of Ki67+ CMs showed an increasing trend both in the border and infarct zones, the only significant difference ($p < 0.05$) was observed between the MI-only and MI + patch + FSTL1 group in the infarct zone (Figure 5E). Within the infarct zone of patch + FSTL1 treated hearts, the number of proliferating CMs was 2.2 and 3.9-fold higher than that in the MI-only and MI + patch groups (Figure 5E, bottom).
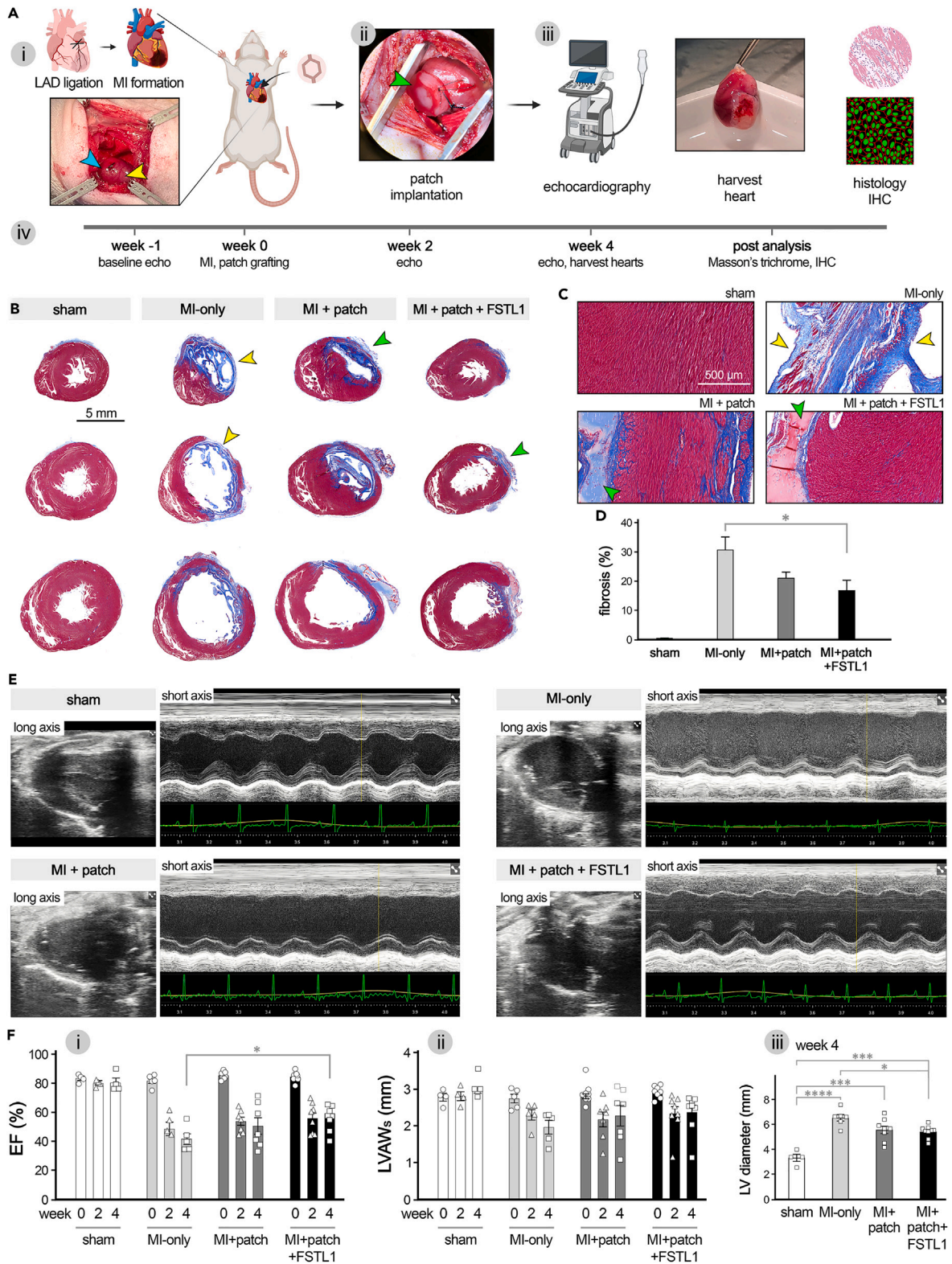
The effect of FSTL1 on vascularization within the patch was shown by endothelial staining with isolectin B4 (IB4) and vWF within the patch area (Figure S1). The staining of endothelial cells within the implanted patches demonstrates more EC presence and circular lumen formation in the FSTL1-loaded patch (Figures S1C, S1D, and S1F) compared to the patch only (Figures S1A, S1B, and S1E).

To determine immune response to the implantation of cardiac patches, rat heart tissues were stained for CD68 macrophage markers within the infarct site (Figure S2A). The number of CD68+ macrophages within the infract zone of each injury group showed no significant difference, suggesting that implantation of bioprinted patches does not increase macrophage infiltration (Figure S2B).

DISCUSSION

Aiming at developing an effective therapeutic device to combat adverse remodeling after MI and regenerate ischemic myocardium, this study utilized a multi-step biofabrication process, consisting of mold-casting and 3D bioprinting, to create functional vascular cardiac patches (Figures 1A–1C). We employed a hybrid bioink, consisting of GelMA, gelatin, and fibrinogen, to create the vascular cardiac patch. As a chemically modified gelatin-based material, GelMA is a versatile bioink due to its stability, tunability, and biocompatibility.[44,45] The methacrylate groups in the GelMA molecular structure can be crosslinked when activated by a photoinitiator and create covalent bonds, providing prolonged mechanical durability of the hydrogel. The structural stability of GelMA allows bioprinting of fine features, such as small vasculature without sacrificing the fidelity. While mechanically stable, GelMA also offers adequate microenvironmental cues for cells to attach, remodel, and proliferate.[46,47] Gelatin solution was added to enhance biological activity of embedded cells and to increase printability of the bioink.[48] The addition of gelatin to GelMA enables maintenance of structural fidelity by keeping the hydrogel stable during the printing process.[49,50] After crosslinking of the printed structure, the sacrificial gelatin component is dissolved out during incubation due to its low melting point and creates micro-scale gaps within the hydrogel.[51] These micro-openings result in reduced elastic modulus of the printed structure and notable increase in surface area for cells to attach and perform biological activities. Furthermore, fibrinogen was mixed into the composite bioink to increase functionality of the hydrogel. As a native ECM protein, fibrin has been widely used in cardiovascular tissue engineering applications due to its biocompatibility and bioactivity.[52] The multi-step biofabrication method implemented in this study, using the hybrid GelMA/gelatin/fibrinogen bioink, loaded with ECs and FSTL1, enabled creating vascular patch devices with physiologically relevant ECM composition and vascular structure (Figure 1).

Figure A (i–iv): Schematic and timeline of experimental procedure — LAD ligation → MI formation, patch implantation, echocardiography, harvest heart, histology/IHC.

iv timeline:
- week -1: baseline echo
- week 0: MI, patch grafting
- week 2: echo
- week 4: echo, harvest hearts
- post analysis: Masson's trichrome, IHC

B sham | MI-only | MI + patch | MI + patch + FSTL1 (5 mm scale)

C Masson's trichrome histology: sham, MI-only, MI + patch, MI + patch + FSTL1 (500 µm scale)

D fibrosis (%): sham, MI-only, MI+patch, MI+patch+FSTL1

E Echocardiography (long axis and short axis): sham, MI-only, MI + patch, MI + patch + FSTL1

F (i) EF (%), (ii) LVAWs (mm), (iii) week 4 LV diameter (mm)

Figure 4. *In vivo* assessment of the engineered cardiac patch function in a rat model of myocardial infarction (MI)

(A) The workflow used for the *in vivo* studies, including the ligation of left anterior descending artery (LAD) artery to induce MI (i), immediate patch grafting to cover the MI and peri-MI regions (ii), and various structural/functional analyses such as echocardiography, and histology (iii). The timeline of the study is presented in (iv).

(B and C) Masson's trichrome staining of harvested heart tissues for four study groups: sham, MI-only, MI + patch, and MI + patch + FSTL1. Consecutive heart sections (from base to apex, B) at week 4 show the viable myocardium (red) and infarct area (blue). Scale bars represent 5 mm (B) and 500 μm (C). Yellow and green arrows point to the ischemic tissue and the patch, respectively.

(D) Quantification of fibrotic tissue percentage of total left ventricular (LV) myocardium at week 4 post treatment, based on the Trichrome staining (n = 5 per group). Data analyzed via one-way ANOVA.

(E) Echocardiogram images of study groups at week 4, showing long axis and short axis views.

(F) Ejection fraction (EF, i) and LV end-systolic anterior wall thickness (LVAWs, ii) measurements at baseline (week 0) and at week 2 and 4 post operation. A sample size of n = 4 was used for the sham group, n = 5 for the MI-only, n = 7 for MI + patch, and n = 8 for MI + patch + FSTL1. Also, LV chamber diameter at week 4 was quantified for different groups using the Trichrome staining images (iii). Data were analyzed using two-way ANOVA for F (i and ii), and using one-way ANOVA for F (iii). A sample size of n = 4 was used for sham, n = 6 for MI-only, n = 8 for MI + patch, and n = 9 for MI + patch + FSTL1. *: $p < 0.05$, **: $p < 0.01$, ***: $p < 0.005$, and ****: $p < 0.001$. Data represent mean ± SEM.

Considering the hybrid nature of patch fabrication workflow, including both 3D bioprinting and casting techniques, assessment of structural fidelity of manufactured devices was of paramount importance. Consistent with our previous studies,[53–56] fabricated constructs demonstrated adequate levels of fidelity, approaching the ratio values of 1.0 for all parameters (Figure 2A). There was, however, a distinct behavior in cellular constructs, in comparison to acellular samples, demonstrating more stable structural features over time. This may be attributed to the different swelling behavior of the two groups.[57] As the hydrogel swells, the empty space within the channels is occupied by the swollen matrix and the channel sizes decrease over time. However, when there are cells encapsulated within the hydrogel, cells can actively remodel the hydrogel, degrade the tissue and deposit their own ECM components, mitigating the swelling effects of the patches.[58]

A common challenge in biofabrication of cardiac tissue analogues is to achieve native-like stiffness (elastic modulus) within the 3D engineered matrix, while maintaining adequate levels of printing fidelity, structural complexity (e.g., vasculature), and cellular functionality.[4,25,59–61] Fine-tuning of crosslinking parameters enabled obtaining a biomimetic range of stiffness in engineered patch constructs (8–18 kPa for cellular and acellular patches, respectively) (Figure 2B). These measurements corresponded with the optimal range of stiffness reported previously to support maximal cardiac cell viability, function, and maturation (1–20 kPa).[62–66] The reduced stiffness in cellular patches, compared to acellular constructs, can be attributed to the role of embedded cells, occupying the spaces in between polymer chains, and preventing a complete crosslinking of GelMA-based bioink.[67] This results in partial polymerization of GelMA and hence, softer cellular patches. We also observed a decreasing trend of stiffness in acellular patches over time, in contrast to increased stiffness of cellular devices at later time points (Figure 2B). This could be explained by the possible swelling of hydrogels and cellular activities/remodeling of the 3D matrix.[68] As the hydrogel swells in culture, the distance between the bioink polymers would increase, leading to weaker connections among polymers and hence, lowered stiffness in the acellular group. The more stable structure and even slight shrinkage in cellular constructs can preserve/strengthen the tightly packed network of bioink polymers. Further, the ECM deposited by the encapsulated cells would serve as fillers for gaps within hydrogel and create ECM network among neighboring cells, resulting in enhanced mechanical properties of cellular patches.[58]

Facilitated mass transport within large (centimeter scale) 3D tissue constructs is another critical requirement for engineered scaffolds to ensure adequate levels of nutrient/waste exchange and cell function.[69] While the bioprinted vascular network within the patch design in this study enhanced the overall blood perfusion within the construct, the micro-pore structure should still allow for interstitial transport of mass within the 3D scaffold. SEM analysis indicated that pore size profile (average pore diameter of 58 μm) was suitable for cell adhesion, migration, and proliferation, as well as the exchange of nutrients and oxygen within the fabricated patch (Figure 2C).[70,71] It should be noted that the SEM sample preparation, specifically the freeze-drying process, resulted in partial deformation and shrinkage of the channels in the SEM images, particularly around the inlet/outlet areas. However, these deformations were not observed in the *in vitro* and *in vivo* assays conducted in this study. It is also likely though that the freeze-drying process affected the pore size in the 3D constructs, due to the freezing step, as well as the negative pressure applied in the chamber, which may result in smaller pore size.[72]

While ECs were encapsulated the bioink to create the bulk patch structure, we also performed a secondary cellularization of these constructs, by manually seeding HUVECs onto the luminal space of bioprinted channels (Figure 3). Patch devices enabled perfusion of media through the printed vasculature, via a bioreactor, simulating blood flow through the vessels in physiological conditions (Figure 3C). The AlamarBlue and IHC analyses of endothelialized patch constructs suggested that the HUVECs remained viable and metabolically active (proliferative) within both patch groups under both static and dynamic culture. The patches exhibited single-layer homogeneous endothelialization of lumen after perfusion. Moreover, the addition of FSTL1 within the patch did not interfere with cellular activities (Figures 3A–3E). FSTL1 peptide is a factor known to promote angiogenesis.[35,73] We therefore examined the angiogenic activity of FSTL1-loaded patches *in vitro*. While the FSTL1 peptide did not yield significant differences in the angiogenic factor levels in the static culture, it upregulated angiogenic activity in the dynamic group (Figures 3F and 3G). This suggests a potential synergistic effect when ECs within 3D patches are exposed to both intravascular flow and the FSTL1. Together, these results indicated that the vascular cardiac patches can be perfused and provide a viable and supportive microenvironment for EC growth and function.

Several previous works, by our group[5] and others,[36,38,42] have demonstrated therapeutic capability of the FSTL1 cardiokine in treating various ischemic heart injuries.[74] This study examined the feasibility and efficacy of FSTL1 incorporation into a vascular bioprinted patch
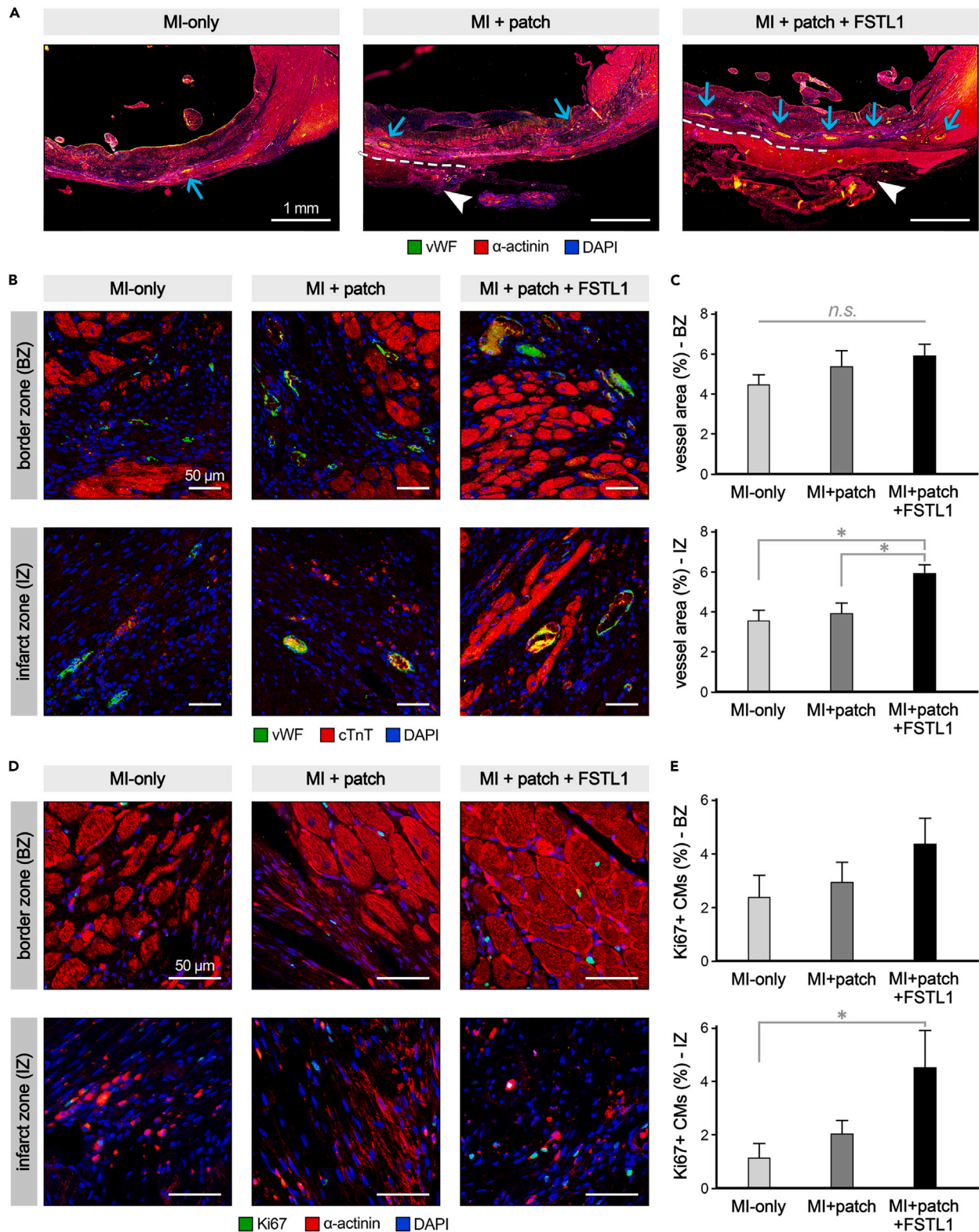
Figure 5. Evaluation of patch-mediated angiogenesis and regeneration of myocardium in the rat model of myocardial infarction (MI)

(A) Representative immunohistochemical (IHC) images of the infarct region in the MI-only, MI + patch, and MI + patch + FSTL1 groups. Staining was performed at week 4 post treatment for α-actinin (red), vWF (green), and DAPI (blue). Scale bars: 1 mm.

Figure 5. *Continued*

(B) IHC analysis of heart/patch sections at week 4, staining for cTnT (red), vWF (green), and DAPI (blue) in the border zone (BZ, top row) and infarct zone (IZ, bottom row). Scale bars: 50 μm.

(C) Quantitative analysis of blood vessel area in BZ (top) and IZ (bottom), based on the IHC images in (B). Groups included MI-only (n = 3), MI + patch (n = 4), and MI + patch + FSTL1 (n = 4).

(D) Expression of α-actinin (red), Ki67 (green), and DAPI (blue) in the border and infarct zones (BZ and IZ in top and bottom rows, respectively). Scale bars: 50 μm.

(E) Quantification of cardiomyocyte (CM) proliferation in the BZ (top) and IZ (bottom) regions. Groups included MI-only (n = 5), MI + patch (n = 5), and MI + patch + FSTL1 (n = 4). *: $p < 0.05$, *n.s.*: not significant. Data represent mean ± SEM and were assessed using one-way ANOVA.

device (Figure 4). The integration of advanced biomanufacturing techniques, perfusable vascular network, and cardioprotective FSTL1 peptide could establish more clinically relevant platforms to create patient and damage specific therapies for MI patients for whom, there are typically no alternative therapies. The longitudinal echocardiography, together with histological and IHC analyses of rat hearts treated with the FSTL1-loaded vascular patch demonstrated the significant impact of the treatment in preventing adverse LV remodeling processes and improving cardiac function (Figures 4 and 5). The cardioprotective function of FSTL1-patch could be driven by multiple mechanisms, including the anti-fibrotic effect (Figures 4B–4D), enhanced angiogenesis and neovascularization (Figures 5A–5C, and S1), and enhanced CM proliferation (Figures 5D and 5E).

There was a ~1.5-fold increase in the vessel area in the patch + FSTL1 treated hearts, compared to the empty patch group, suggesting that the FSTL1 peptide laden in the patch was the primary contributor to the neovascularization of the infarct tissue (Figure 5C). We also examined neovascularization inside the patch structure (Figure S1) which demonstrated noticeably higher levels of EC staining and evidence of lumen formation in the patch + FSTL1 compared with the patch − FSTL1 group (red arrows, Figures S1C and S1D). These results are consistent with previous reports on the angiogenic activity of FSTL1 chemokine,[34,35,73,75] and signify the important role of FSTL1-loaded cardiac patch treatment in promoting neovascularization within the injury site.

IHC analysis of harvested hearts also demonstrated the significant effect of FSTL1-patch treatment in promoting native CMs proliferation (increase in Ki67+ CMs), particularly in the infarct zone (Figure 5E). Although, the increased Ki67 signal may indicate DNA synthesis without cell division,[76] and therefore, warrants further research. The enhanced CM proliferation, along with the boosted neovascularization, demonstrated that the endothelialized vascular patch, laden with FSTL1, offered the highest cardioprotective and regenerative outcome for the ischemic heart tissue. These regenerative responses at cellular level could explain the reduced remodeling of the LV (fibrotic scar formation, LV dilation, and wall thinning) and preserved cardiac function after the patch + FSTL1 treatment.

Considering the significant role that the FSTL1 glycoprotein plays in the regulation of the immune and inflammatory responses,[34,77,78] we also examined the effect of FSTL1-patch therapy on the macrophage population in the heart sections (Figure S2). IHC imaging of macrophages (CD68, red) and CMs (cTnT, green) demonstrated no significant differences ($p > 0.05$) of CD68+ cells showed no significant differences between MI-only and patch treated groups (with and without FSTL1). These results suggested that the FSTL1-patch treatment did not elicit significant inflammatory response, which was in agreement with prior reports.[5]

In summary, the results observed from this study highlight the promising impact of 3D bioprinted cardiac patch devices, loaded with vascular cells and pro-proliferative molecules, to support regeneration of the myocardium after MI. Considering the biocompatibility of the hydrogel and tunability of the manufacturing process, these 3D vascular cardiac patches can be further utilized to deliver other types of cells and molecules to the injury site and direct remuscularization of the heart.[79–82] Furthermore, the cellularized vascular constructs can be used as a 3D *in vitro* model to investigate various cellular responses to different stimuli and therapeutics in the context of physiological or pathophysiological processes in the human cardiovascular system.

Limitations of the study

In the present study, the printed vasculature within the patch was not connected to the native vasculature in the myocardium due to the technical difficulty of the surgical anastomosis in the rat model. Conducting future patch studies in larger animal models could allow the direct anastomosis of the channels win the patch with the host tissue vasculature, hence, enabling more effective engraftment and blood perfusion within the patch. Future studies could also more closely examine the stability and patency of printed channels within the patch, following implantation *in vivo*. It should be noted that the increased Ki67 signal may reflect increased DNA synthesis and polyploidy in the CMs, independent from the cell division (Ki67 is expressed in all cell cycle phases including the mitotic events).[76] Therefore, future in-depth analysis of CM proliferation using late cytokinesis markers (e.g., aurora B) would be needed to further confirm the pro-proliferative effect of patch therapy.[5] Further studies could also examine the cascade of inflammatory events in more detail and at serial time points post MI/treatment. Finally, evaluating the function of FSTL1-laden patch in larger animal models of acute and chronic MI (e.g., ischemia reperfusion injury[83]), and in immune compatible models, would be of great importance to assess the potential of the developed therapy for clinical translation. Delayed application of the patch (e.g., one week post injury) in the chronic model would offer more clinical relevance for the translation of the biofabricated vascular patch.

RESOURCE AVAILABILITY

Lead contact

Any further information and requests for resources and reagents should be directed to and will be fulfilled by the lead contact, Vahid Serpooshan (vahid.serpoosahan@bme.gatech.edu).

CellPress
OPEN ACCESS

Materials availability

This study did not generate new unique reagents.

Data and code availability

- Any data reported in this paper will be shared by the lead contact upon request.
- No original code was generated in this study.
- Any additional information required to reanalyze the data reported in this paper is available from the lead contact upon request.

AUTHOR CONTRIBUTIONS

Conceptualization, B.H. and V.S.; methodology, B.H., M.S., and V.S.; investigation, data collection, and analysis, B.H., L.K., M.S., L.J., Y.S., and M.A.; writing – original draft, B.H.; writing – review and editing, B.H. and V.S.; funding acquisition, V.S.; resources, H.B.-H. and V.S.; supervision, H.B.-H. and V.S.

DECLARATION OF INTERESTS

V.S. is an inventor on a patent describing a cast collagen patch to deliver FSTL1 for the treatment of myocardial infarction (US Patent 14,168,826). Vahid Serpooshan is a consulting academic editor at iScience and serves as one of the Guest Editors of the Special Issue "Advanced biomanufacturing of cardiovascular tissues".

STAR★METHODS

Detailed methods are provided in the online version of this paper and include the following:

- KEY RESOURCES TABLE
- EXPERIMENTAL MODEL AND STUDY PARTICIPANT DETAILS
    - HUVEC culture
    - Bioink preparation
    - Design and biofabrication of cardiac patch constructs
    - Endothelialization and *in vitro* culture of patch constructs
    - Creating the rat model of MI – Application of cardiac patch
- METHOD DETAILS
    - Structural fidelity and stability assessment of patch constructs
    - Micromechanical characterization of patch constructs
    - Ultrastructural analysis – Pore size measurement
    - AlamarBlue metabolic activity assay
    - Immunofluorescent staining of *in vitro* patch constructs
    - Angiogenesis microarray analysis
    - Echocardiography
    - Histology and immunohistochemical analysis of patch-treated hearts
- QUANTIFICATION AND STATISTICAL ANALYSIS

SUPPLEMENTAL INFORMATION

Supplemental information can be found online at https://doi.org/10.1016/j.isci.2024.110770.

REFERENCES

1. Hashimoto, H., Olson, E.N., and Bassel-Duby, R. (2018). Therapeutic approaches for cardiac regeneration and repair. Nat. Rev. Cardiol. *15*, 585–600. https://doi.org/10.1038/s41569-018-0036-6.

2. Doppler, S.A., Deutsch, M.A., Serpooshan, V., Li, G., Dzilic, E., Lange, R., Krane, M., and Wu, S.M. (2017). Mammalian Heart Regeneration: The Race to the Finish Line. Circ. Res. *120*, 630–632. https://doi.org/10.1161/CIRCRESAHA.116.310051.

3. Mahmoudi, M., Yu, M., Serpooshan, V., Wu, J.C., Langer, R., Lee, R.T., Karp, J.M., and Farokhzad, O.C. (2017). Multiscale technologies for treatment of ischemic cardiomyopathy. Nat. Nanotechnol. *12*, 845–855. https://doi.org/10.1038/nnano.2017.167.

4. Wang, L., Serpooshan, V., and Zhang, J. (2021). Engineering Human Cardiac Muscle Patch Constructs for Prevention of Post-infarction LV Remodeling. Front. Cardiovasc. Med. *8*, 621781. https://doi.org/10.3389/fcvm.2021.621781.

5. Wei, K., Serpooshan, V., Hurtado, C., Diez-Cuñado, M., Zhao, M., Maruyama, S., Zhu, W., Fajardo, G., Noseda, M., Nakamura, K., et al. (2015). Epicardial FSTL1 reconstitution regenerates the adult mammalian heart. Nature *525*, 479–485. https://doi.org/10.1038/nature15372.

6. Serpooshan, V., Zhao, M., Metzler, S.A., Wei, K., Shah, P.B., Wang, A., Mahmoudi, M.,

Malkovskiy, A.V., Rajadas, J., Butte, M.J., et al. (2014). Use of bio-mimetic three-dimensional technology in therapeutics for heart disease. Bioengineered *5*, 193–197. https://doi.org/10.4161/bioe.27751.

7. Serpooshan, V., Zhao, M., Metzler, S.A., Wei, K., Shah, P.B., Wang, A., Mahmoudi, M., Malkovskiy, A.V., Rajadas, J., Butte, M.J., et al. (2013). The effect of bioengineered acellular collagen patch on cardiac remodeling and ventricular function post myocardial infarction. Biomaterials *34*, 9048–9055. https://doi.org/10.1016/j.biomaterials.2013.08.017.

8. Zhang, Y., Mu, W., Zhang, Y., He, X., Wang, Y., Ma, H., Zhu, T., Li, A., Hou, Q., Yang, W., et al. (2022). Recent Advances in Cardiac Patches: Materials, Preparations, and Properties. ACS Biomater. Sci. Eng. *8*, 3659–3675. https://doi.org/10.1021/acsbiomaterials.2c00348.

9. Taylor, D.A., Sampaio, L.C., and Gobin, A. (2014). Building New Hearts: A Review of Trends in Cardiac Tissue Engineering. Am. J. Transplant. *14*, 2448–2459. https://doi.org/10.1111/ajt.12939.

10. D'Amore, A., Yoshizumi, T., Luketich, S.K., Wolf, M.T., Gu, X., Cammarata, M., Hoff, R., Badylak, S.F., and Wagner, W.R. (2016). Bi-layered polyurethane - Extracellular matrix cardiac patch improves ischemic ventricular wall remodeling in a rat model. Biomaterials *107*, 1–14. https://doi.org/10.1016/j.biomaterials.2016.07.039.

11. Vunjak-Novakovic, G., Tandon, N., Godier, A., Maidhof, R., Marsano, A., Martens, T.P., and Radisic, M. (2010). Challenges in Cardiac Tissue Engineering. Tissue Eng. Part B-Re *16*, 169–187. https://doi.org/10.1089/ten.teb.2009.0352.

12. Cho, S., Discher, D.E., Leong, K.W., Vunjak-Novakovic, G., and Wu, J.C. (2022). Challenges and opportunities for the next generation of cardiovascular tissue engineering. Nat. Methods *19*, 1064–1071. https://doi.org/10.1038/s41592-022-01591-3.

13. Zhang, J., Tomov, M.L., Chong, J.J.H., Menasché, P., and Serpooshan, V. (2021). Editorial: Bioengineering and Biotechnology Approaches in Cardiovascular Sciences. Front. Bioeng. Biotechnol. *9*, 746435. https://doi.org/10.3389/fbioe.2021.746435.

14. Serpooshan, V., Chen, P., Wu, H., Lee, S., Sharma, A., Hu, D.A., Venkatraman, S., Ganesan, A.V., Usta, O.B., Yarmush, M., et al. (2017). Bioacoustic-enabled patterning of human iPSC-derived cardiomyocytes into 3D cardiac tissue. Biomaterials *131*, 47–57. https://doi.org/10.1016/j.biomaterials.2017.03.037.

15. Richards, D., Jia, J., Yost, M., Markwald, R., and Mei, Y. (2017). 3D Bioprinting for Vascularized Tissue Fabrication. Ann. Biomed. Eng. *45*, 132–147. https://doi.org/10.1007/s10439-016-1653-z.

16. Rademakers, T., Horvath, J.M., van Blitterswijk, C.A., and LaPointe, V.L.S. (2019). Oxygen and nutrient delivery in tissue engineering: Approaches to graft vascularization. J. Tissue Eng. Regen. Med. *13*, 1815–1829. https://doi.org/10.1002/term.2932.

17. Noor, N., Shapira, A., Edri, R., Gal, I., Wertheim, L., and Dvir, T. (2019). 3D Printing of Personalized Thick and Perfusable Cardiac Patches and Hearts. Adv. Sci. *6*, 1900344. https://doi.org/10.1002/advs.201900344.

18. Roux, B.M., Akar, B., Zhou, W., Stojkova, K., Barrera, B., Brankov, J., and Brey, E.M. (2018). Preformed Vascular Networks Survive and Enhance Vascularization in Critical Sized Cranial Defects. Tissue Eng. *24*, 1603–1615. https://doi.org/10.1089/ten.TEA.2017.0493.

19. Novosel, E.C., Kleinhans, C., and Kluger, P.J. (2011). Vascularization is the key challenge in tissue engineering. Adv. Drug Deliv. Rev. *63*, 300–311. https://doi.org/10.1016/j.addr.2011.03.004.

20. Su, T., Huang, K., Mathews, K.G., Scharf, V.F., Hu, S., Li, Z., Frame, B.N., Cores, J., Dinh, P.U., Daniele, M.A., et al. (2020). Cardiac Stromal Cell Patch Integrated with Engineered Microvessels Improves Recovery from Myocardial Infarction in Rats and Pigs. ACS Biomater. Sci. Eng. *6*, 6309–6320. https://doi.org/10.1021/acsbiomaterials.0c00942.

21. Schaefer, J.A., Guzman, P.A., Riemenschneider, S.B., Kamp, T.J., and Tranquillo, R.T. (2018). A cardiac patch from aligned microvessel and cardiomyocyte patches. J. Tissue Eng. Regen. Med. *12*, 546–556. https://doi.org/10.1002/term.2568.

22. Redd, M.A., Zeinstra, N., Qin, W., Wei, W., Martinson, A., Wang, Y., Wang, R.K., Murry, C.E., and Zheng, Y. (2019). Patterned human microvascular grafts enable rapid vascularization and increase perfusion in infarcted rat hearts. Nat. Commun. *10*, 584. https://doi.org/10.1038/s41467-019-08388-7.

23. Zhang, Z., Xu, C., Xu, L., Wan, J., Cao, G., Liu, Z., Ji, P., Jin, Q., Fu, Y., Le, Y., et al. (2024). Bioprinted dermis with human adipose tissue-derived microvascular fragments promotes wound healing. Biotechnol. Bioeng. *121*, 1407–1421. https://doi.org/10.1002/bit.28588.

24. Sarker, M.D., Naghieh, S., Sharma, N.K., and Chen, X. (2018). 3D biofabrication of vascular networks for tissue regeneration: A report on recent advances. J. Pharm. Anal. *8*, 277–296. https://doi.org/10.1016/j.jpha.2018.08.005.

25. Serpooshan, V., and Zhang, J. (2022). Advanced Technologies in Cardiovascular Bioengineering, 1 Edition (Springer Cham). https://doi.org/10.1007/978-3-030-86140-7.

26. Li, M.T., Ruehle, M.A., Stevens, H.Y., Servies, N., Willett, N.J., Karthikeyakannan, S., Warren, G.L., Guldberg, R.E., and Krishnan, L. (2017). Skeletal Myoblast-Seeded Vascularized Tissue Scaffolds in the Treatment of a Large Volumetric Muscle Defect in the Rat Biceps Femoris Muscle. Tissue Eng. *23*, 989–1000. https://doi.org/10.1089/ten.tea.2016.0523.

27. Laschke, M.W., and Menger, M.D. (2022). Microvascular Fragments in Microcirculation Research and Regenerative Medicine. Tissue Eng., Part B *28*, 1109–1120. https://doi.org/10.1089/ten.teb.2021.0160.

28. Qian, Z., Sharma, D., Jia, W., Radke, D., Kamp, T., and Zhao, F. (2019). Engineering stem cell cardiac patch with microvascular features representative of native myocardium. Theranostics *9*, 2143–2157. https://doi.org/10.7150/thno.29552.

29. Roche, C.D., Sharma, P., Ashton, A.W., Jackson, C., Xue, M., and Gentile, C. (2021). Printability, Durability, Contractility and Vascular Network Formation in 3D Bioprinted Cardiac Endothelial Cells Using Alginate-Gelatin Hydrogels. Front. Bioeng. Biotechnol. *9*, 636257. https://doi.org/10.3389/fbioe.2021.636257.

30. Jang, J., Park, H.J., Kim, S.W., Kim, H., Park, J.Y., Na, S.J., Kim, H.J., Park, M.N., Choi, S.H., Park, S.H., et al. (2017). 3D printed complex tissue construct using stem cell-laden decellularized extracellular matrix bioinks for cardiac repair. Biomaterials *112*, 264–274. https://doi.org/10.1016/j.biomaterials.2016.10.026.

31. Cetnar, A.D., Tomov, M.L., Ning, L., Jing, B., Theus, A.S., Kumar, A., Wijntjes, A.N., Bhamidipati, S.R., Do, K.P., Mantalaris, A., et al. (2021). Patient-Specific 3D Bioprinted Models of Developing Human Heart. Adv. Healthcare Mater. *10*, e2001169. https://doi.org/10.1002/adhm.202001169.

32. Tomov, M.L., Gil, C.J., Cetnar, A., Theus, A.S., Lima, B.J., Nish, J.E., Bauser-Heaton, H.D., and Serpooshan, V. (2019). Engineering Functional Cardiac Tissues for Regenerative Medicine Applications. Curr. Cardiol. Rep. *21*, 105. https://doi.org/10.1007/s11886-019-1178-9.

33. Tomov, M.L., Perez, L., Ning, L., Chen, H., Jing, B., Mingee, A., Ibrahim, S., Theus, A.S., Kabboul, G., Do, K., et al. (2021). A 3D Bioprinted In Vitro Model of Pulmonary Artery Atresia to Evaluate Endothelial Cell Response to Microenvironment. Adv. Healthcare Mater. *10*, e2100968. https://doi.org/10.1002/adhm.202100968.

34. Mattiotti, A., Prakash, S., Barnett, P., and van den Hoff, M.J.B. (2018). Follistatin-like 1 in development and human diseases. Cell. Mol. Life Sci. *75*, 2339–2354. https://doi.org/10.1007/s00018-018-2805-0.

35. Ouchi, N., Oshima, Y., Ohashi, K., Higuchi, A., Ikegami, C., Izumiya, Y., and Walsh, K. (2008). Follistatin-like 1, a Secreted Muscle Protein, Promotes Endothelial Cell Function and Revascularization in Ischemic Tissue through a Nitric-oxide Synthase-dependent Mechanism. J. Biol. Chem. *283*, 32802–32811. https://doi.org/10.1074/jbc.M803440200.

36. Peters, M.C., Di Martino, S., Boelens, T., Qin, J., van Mil, A., Doevendans, P.A., Chamuleau, S.A.J., Sluijter, J.P.G., and Neef, K. (2022). Follistatin-like 1 promotes proliferation of matured human hypoxic iPSC-cardiomyocytes and is secreted by cardiac fibroblasts. Mol. Ther. Methods Clin. Dev. *25*, 3–16. https://doi.org/10.1016/j.omtm.2022.02.005.

37. Shimano, M., Ouchi, N., Nakamura, K., van Wijk, B., Ohashi, K., Asaumi, Y., Higuchi, A., Pimentel, D.R., Sam, F., Murohara, T., et al. (2011). Cardiac myocyte follistatin-like 1 functions to attenuate hypertrophy following pressure overload. Proc. Natl. Acad. Sci. USA *108*, E899–E906. https://doi.org/10.1073/pnas.1108592108.

38. Maruyama, S., Nakamura, K., Papanicolaou, K.N., Sano, S., Shimizu, I., Asaumi, Y., van den Hoff, M.J., Ouchi, N., Recchia, F.A., and Walsh, K. (2016). Follistatin-like 1 promotes cardiac fibroblast activation and protects the heart from rupture. EMBO Mol. Med. *8*, 949–966. https://doi.org/10.15252/emmm.201506151.

39. Jiang, X., Feng, T., An, B., Ren, S., Meng, J., Li, K., Liu, S., Wu, H., Zhang, H., and Zhong, C. (2022). A Bi-Layer Hydrogel Cardiac Patch Made of Recombinant Functional Proteins. Adv. Mater. *34*, 2201411. https://doi.org/10.1002/adma.202201411.

40. Shen, H., Cui, G., Li, Y., Ye, W., Sun, Y., Zhang, Z., Li, J., Xu, G., Zeng, X., Zhang, Y., et al. (2019). Follistatin-like 1 protects mesenchymal stem cells from hypoxic damage and enhances their therapeutic efficacy in a mouse myocardial infarction model. Stem Cell Res. Ther. *10*, 17. https://doi.org/10.1186/s13287-018-1111-y.

41. Serpooshan, V., and Ruiz-Lozano, P. (2014). Ultra-rapid manufacturing of engineered

epicardial substitute to regenerate cardiac tissue following acute ischemic injury. Methods Mol. Biol. *1210*, 239–248. https://doi.org/10.1007/978-1-4939-1435-7_18.

42. Altekoester, A.K., and Harvey, R.P. (2015). Bioengineered FSTL1 Patches Restore Cardiac Function Following Myocardial Infarction. Trends Mol. Med. *21*, 731–733. https://doi.org/10.1016/j.molmed.2015.10.006.

43. van Amerongen, M.J., and Engel, F.B. (2008). Features of cardiomyocyte proliferation and its potential for cardiac regeneration. J. Cell Mol. Med. *12*, 2233–2244. https://doi.org/10.1111/j.1582-4934.2008.00439.x.

44. Zhu, M., Wang, Y., Ferracci, G., Zheng, J., Cho, N.J., and Lee, B.H. (2019). Gelatin methacryloyl and its hydrogels with an exceptional degree of controllability and batch-to-batch consistency. Sci. Rep. *9*, 6863. https://doi.org/10.1038/s41598-019-42186-x.

45. Bolonduro, O.A., Duffy, B.M., Rao, A.A., Black, L.D., and Timko, B.P. (2020). From biomimicry to bioelectronics: Smart materials for cardiac tissue engineering. Nano Res. *13*, 1253–1267. https://doi.org/10.1007/s12274-020-2682-3.

46. Yue, K., Trujillo-de Santiago, G., Alvarez, M.M., Tamayol, A., Annabi, N., and Khademhosseini, A. (2015). Synthesis, properties, and biomedical applications of gelatin methacryloyl (GelMA) hydrogels. Biomaterials *73*, 254–271. https://doi.org/10.1016/j.biomaterials.2015.08.045.

47. Ying, G., Jiang, N., Yu, C., and Zhang, Y.S. (2018). Three-dimensional bioprinting of gelatin methacryloyl (GelMA). Bio-Des. Manuf. *1*, 215–224. https://doi.org/10.1007/s42242-018-0028-8.

48. Freeman, S., Ramos, R., Alexis Chando, P., Zhou, L., Reeser, K., Jin, S., Soman, P., and Ye, K. (2019). A bioink blend for rotary 3D bioprinting tissue engineered small-diameter vascular constructs. Acta Biomater. *95*, 152–164. https://doi.org/10.1016/j.actbio.2019.06.052.

49. Yin, J., Yan, M., Wang, Y., Fu, J., and Suo, H. (2018). 3D Bioprinting of Low-Concentration Cell-Laden Gelatin Methacrylate (GelMA) Bioinks with a Two-Step Cross-linking Strategy. ACS Appl. Mater. Interfaces *10*, 6849–6857. https://doi.org/10.1021/acsami.7b16059.

50. Riffe, M.B., Davidson, M.D., Seymour, G., Dhand, A.P., Cooke, M.E., Zlotnick, H.M., McLeod, R.R., and Burdick, J.A. (2024). Multi-Material Volumetric Additive Manufacturing of Hydrogels using Gelatin as a Sacrificial Network and 3D Suspension Bath. Adv. Mater. *36*, e2309026. https://doi.org/10.1002/adma.202309026.

51. Ouyang, L., Armstrong, J.P.K., Chen, Q., Lin, Y., and Stevens, M.M. (2020). Void-Free 3D Bioprinting for In Situ Endothelialization and Microfluidic Perfusion. Adv. Funct. Mater. *30*, 1908349. https://doi.org/10.1002/adfm.201908349.

52. de Melo, B.A.G., Jodat, Y.A., Cruz, E.M., Benincasa, J.C., Shin, S.R., and Porcionatto, M.A. (2020). Strategies to use fibrinogen as bioink for 3D bioprinting fibrin-based soft and hard tissues. Acta Biomater. *117*, 60–76. https://doi.org/10.1016/j.actbio.2020.09.024.

53. Ning, L., Zanella, S., Tomov, M.L., Amoli, M.S., Jin, L., Hwang, B., Saadeh, M., Chen, H., Neelakantan, L., Dasi, L.P., et al. (2024). Targeted Rapamycin Delivery via Magnetic Nanoparticles to Address Stenosis in a 3D Bioprinted in Vitro Model of Pulmonary Veins.

Adv. Sci. *11*, e2400476. https://doi.org/10.1002/advs.202400476.

54. Chen, S., Tomov, M.L., Ning, L., Gil, C.J., Hwang, B., Bauser-Heaton, H.D., Chen, H., and Serpooshan, V. (2023). 3D bioprinting of adhesive hybrid hydrogel scaffolds for tissue engineering applications. Advanced Biology *59*, 9021–9041.

55. Gil, C.J., Evans, C.J., Li, L., Allphin, A.J., Tomov, M.L., Jin, L., Vargas, M., Hwang, B., Wang, J., Putaturo, V., et al. (2023). Leveraging 3d Bioprinting And Photon-Counting Computed Tomography to Enable Noninvasive Quantitative Tracking of Multifunctional Tissue Engineered Constructs. Adv. Healthcare Mater. *12*, e2302271. https://doi.org/10.1002/adhm.202302271.

56. Ning, L., Shim, J., Tomov, M.L., Liu, R., Mehta, R., Mingee, A., Hwang, B., Jin, L., Mantalaris, A., Xu, C., et al. (2022). A 3D Bioprinted in vitro Model of Neuroblastoma Recapitulates Dynamic Tumor-Endothelial Cell Interactions Contributing to Solid Tumor Aggressive Behavior. Adv. Sci. *9*, e2200244. https://doi.org/10.1002/advs.202200244.

57. Zhan, Y., Fu, W., Xing, Y., Ma, X., and Chen, C. (2021). Advances in versatile anti-swelling polymer hydrogels. Mater. Sci. Eng., C *127*, 112208. https://doi.org/10.1016/j.msec.2021.112208.

58. Tibbitt, M.W., and Anseth, K.S. (2009). Hydrogels as Extracellular Matrix Mimics for 3D Cell Culture. Biotechnol. Bioeng. *103*, 655–663. https://doi.org/10.1002/bit.22361.

59. Tomov, M.L., Vargas, M., Gil, C.J., Theus, A.S., Cetnar, A.C., Pham Do, K., Veneziano, R., and Serpooshan, V. (2020). Chapter 12 - Nano-bioink solutions for cardiac tissue bioprinting. In Nanomedicine for Ischemic Cardiomyopathy, M. Mahmoudi, ed. (Academic Press), pp. 171–185. https://doi.org/10.1016/B978-0-12-817434-0.00012-X.

60. Cetnar, A., Tomov, M., Theus, A., Lima, B., Vaidya, A., and Serpooshan, V. (2019). 3D Bioprinting in Clinical Cardiovascular Medicine. In 3D Bioprinting in Medicine: Technologies, Bioinks, and Applications, M. Guvendiren, ed. (Springer International Publishing), pp. 149–162. https://doi.org/10.1007/978-3-030-23906-0_5.

61. Tomov, M.L., Theus, A., Sarasani, R., Chen, H., and Serpooshan, V. (2019). 3D Bioprinting of Cardiovascular Tissue Constructs: Cardiac Bioinks. In Cardiovascular Regenerative Medicine: Tissue Engineering and Clinical Applications, V. Serpooshan and S.M. Wu, eds. (Springer International Publishing), pp. 63–77. https://doi.org/10.1007/978-3-030-20047-3_4.

62. Tallawi, M., Rai, R., Boccaccini, A.R., and Aifantis, K.E. (2015). Effect of substrate mechanics on cardiomyocyte maturation and growth. Tissue Eng., Part B *21*, 157–165. https://doi.org/10.1089/ten.TEB.2014.0383.

63. Amdursky, N., Mazo, M.M., Thomas, M.R., Humphrey, E.J., Puetzer, J.L., St-Pierre, J.P., Skaalure, S.C., Richardson, R.M., Terracciano, C.M., and Stevens, M.M. (2018). Elastic serum-albumin based hydrogels: mechanism of formation and application in cardiac tissue engineering. J. Mater. Chem. B *6*, 5604–5612. https://doi.org/10.1039/C8TB01014E.

64. Pandey, P., Hawkes, W., Hu, J., Megone, W.V., Gautrot, J., Anilkumar, N., Zhang, M., Hirvonen, L., Cox, S., Ehler, E., et al. (2018). Cardiomyocytes Sense Matrix Rigidity through a Combination of Muscle and Non-muscle Myosin Contractions. Dev. Cell *45*,

661. https://doi.org/10.1016/j.devcel.2018.05.016.

65. Hu, J.B., Hu, D.A., Buikema, J.W., Chirikian, O., Venkatraman, S., Serpooshan, V., and Wu, S.M. (2017). Bioengineering of vascular myocardial tissue; a 3D bioprinting approach. Tissue Eng. *23*, S158–S159.

66. Lee, S., Serpooshan, V., Tong, X., Venkatraman, S., Lee, M., Lee, J., Chirikian, O., Wu, J.C., Wu, S.M., and Yang, F. (2017). Contractile force generation by 3D hiPSC-derived cardiac tissues is enhanced by rapid establishment of cellular interconnection in matrix with muscle-mimicking stiffness. Biomaterials *131*, 111–120. https://doi.org/10.1016/j.biomaterials.2017.03.039.

67. Rivero, R.E., Capella, V., Cecilia Liaudat, A., Bosch, P., Barbero, C.A., Rodríguez, N., and Rivarola, C.R. (2020). Mechanical and physicochemical behavior of a 3D hydrogel scaffold during cell growth and proliferation. RSC Adv. *10*, 5827–5837. https://doi.org/10.1039/c9ra08162c.

68. Kesselman, D., Kossover, O., Mironi-Harpaz, I., and Seliktar, D. (2013). Time-dependent cellular morphogenesis and matrix stiffening in proteolytically responsive hydrogels. Acta Biomater. *9*, 7630–7639. https://doi.org/10.1016/j.actbio.2013.04.030.

69. Mekala, N.K., Baadhe, R.R., and Potumarthi, R. (2014). Mass transfer aspects of 3D cell cultures in tissue engineering. Asia Pac. J. Chem. Eng. *9*, 318–329. https://doi.org/10.1002/apj.1800.

70. Bruzauskaite, I., Bironaite, D., Bagdonas, E., and Bernotiene, E. (2016). Scaffolds and cells for tissue regeneration: different scaffold pore sizes-different cell effects. Cytotechnology *68*, 355–369. https://doi.org/10.1007/s10616-015-9895-4.

71. Chiu, Y.C., Cheng, M.H., Engel, H., Kao, S.W., Larson, J.C., Gupta, S., and Brey, E.M. (2011). The role of pore size on vascularization and tissue remodeling in PEG hydrogels. Biomaterials *32*, 6045–6051. https://doi.org/10.1016/j.biomaterials.2011.04.066.

72. O'Brien, F.J., Harley, B.A., Yannas, I.V., and Gibson, L. (2004). Influence of freezing rate on pore structure in freeze-dried collagen-GAG scaffolds. Biomaterials *25*, 1077–1086. https://doi.org/10.1016/s0142-9612(03)00630-6.

73. Xi, Y., Gong, D.W., and Tian, Z. (2016). FSTL1 as a Potential Mediator of Exercise-Induced Cardioprotection in Post-Myocardial Infarction Rats. Sci. Rep. *6*, 32424. https://doi.org/10.1038/srep32424.

74. Crunkhorn, S. (2015). Cardiovascular disease: Patching up the heart. Nat. Rev. Drug Discov. *14*, 747. https://doi.org/10.1038/nrd4764.

75. Li, M.Y., Gao, R.P., Zhu, Q., Chen, Y., Tao, B.B., and Zhu, Y.C. (2023). Skeletal muscle-derived FSTL1 starting up angiogenesis by regulating endothelial junction via activating Src pathway can be upregulated by hydrogen sulfide. Am. J. Physiol. Cell Physiol. *325*, C1252-c1266. https://doi.org/10.1152/ajpcell.00219.2023.

76. Alkass, K., Panula, J., Westman, M., Wu, T.D., Guerquin-Kern, J.L., and Bergmann, O. (2015). No Evidence for Cardiomyocyte Number Expansion in Preadolescent Mice. Cell *163*, 1026–1036. https://doi.org/10.1016/j.cell.2015.10.035.

77. Li, X., Fang, Y., Jiang, D., Dong, Y., Liu, Y., Zhang, S., Guo, J., Qi, C., Zhao, C., Jiang, F., et al. (2021). Targeting FSTL1 for Multiple Fibrotic and Systemic Autoimmune Diseases.

Mol. Ther. *29*, 347–364. https://doi.org/10.1016/j.ymthe.2020.09.031.

78. Chen, L., and Liu, Z. (2019). Downregulation of FSTL-1 attenuates the inflammation injury during Streptococcus pneumoniae infection by inhibiting the NLRP3 and TLR4/NF-kappaB signaling pathway. Mol. Med. Rep. *20*, 5345–5352. https://doi.org/10.3892/mmr.2019.10752.

79. Das, S., Nam, H., and Jang, J. (2021). 3D bioprinting of stem cell-laden cardiac patch: A promising alternative for myocardial repair. APL Bioeng. *5*, 031508. https://doi.org/10.1063/5.0030353.

80. Ong, C.S., Nam, L., Ong, K., Krishnan, A., Huang, C.Y., Fukunishi, T., and Hibino, N. (2018). 3D and 4D Bioprinting of the Myocardium: Current Approaches, Challenges, and Future Prospects. BioMed Res. Int. *2018*, 6497242. https://doi.org/10.1155/2018/6497242.

81. Zhang, J., Zhu, W., Radisic, M., and Vunjak-Novakovic, G. (2018). Can We Engineer a Human Cardiac Patch for Therapy? Circ. Res. *123*, 244–265. https://doi.org/10.1161/Circresaha.118.311213.

82. Bejleri, D., Streeter, B.W., Nachlas, A.L.Y., Brown, M.E., Gaetani, R., Christman, K.L., and Davis, M.E. (2018). A Bioprinted Cardiac Patch Composed of Cardiac-Specific Extracellular Matrix and Progenitor Cells for Heart Repair. Adv. Healthcare Mater. *7*, e1800672. https://doi.org/10.1002/adhm.201800672.

83. Liu, T., Hao, Y., Zhang, Z., Zhou, H., Peng, S., Zhang, D., Li, K., Chen, Y., and Chen, M. (2024). Advanced Cardiac Patches for the Treatment of Myocardial Infarction. Circulation *149*, 2002–2020. https://doi.org/10.1161/CIRCULATIONAHA.123.067097.

84. Ning, L., Mehta, R., Cao, C., Theus, A., Tomov, M., Zhu, N., Weeks, E.R., Bauser-Heaton, H., and Serpooshan, V. (2020). Embedded 3D Bioprinting of Gelatin Methacryloyl-Based Constructs with Highly Tunable Structural Fidelity. ACS Appl. Mater. Interfaces *12*, 44563–44577. https://doi.org/10.1021/acsami.0c15078.

85. Theus, A.S., Ning, L., Kabboul, G., Hwang, B., Tomov, M.L., LaRock, C.N., Bauser-Heaton, H., Mahmoudi, M., and Serpooshan, V. (2022). 3D bioprinting of nanoparticle-laden hydrogel scaffolds with enhanced antibacterial and imaging properties. iScience *25*, 104947. https://doi.org/10.1016/j.isci.2022.104947.

86. Li, L., Gil, C.J., Finamore, T.A., Evans, C.J., Tomov, M.L., Ning, L., Theus, A., Kabboul, G., Serpooshan, V., and Roeder, R.K. (2022). Methacrylate-Modified Gold Nanoparticles Enable Non-Invasive Monitoring of Photocrosslinked Hydrogel Scaffolds. Adv. Nanobiomed Res. *2*, 2200022. https://doi.org/10.1002/anbr.202200022.

87. Oliver, W.C., and Pharr, G.M. (2004). Measurement of hardness and elastic modulus by instrumented indentation: Advances in understanding and refinements to methodology. J. Mater. Res. *19*, 3–20.

88. Oliver, W.C., and Pharr, G.M. (1992). An improved technique for determining hardness and elastic modulus using load and displacement sensing indentation experiments. J. Mater. Res. *7*, 1564–1583.

89. Serpooshan, V., Quinn, T.M., Muja, N., and Nazhat, S.N. (2011). Characterization and modelling of a dense lamella formed during self-compression of fibrillar collagen gels: implications for biomimetic scaffolds. Soft Matter *7*, 2918–2926. https://doi.org/10.1039/c0sm00691b.

90. Serpooshan, V., Muja, N., Marelli, B., and Nazhat, S.N. (2011). Fibroblast contractility and growth in plastic compressed collagen gel scaffolds with microstructures correlated with hydraulic permeability. J. Biomed. Mater. Res. *96*, 609–620. https://doi.org/10.1002/jbm.a.33008.

91. Serpooshan, V., Julien, M., Nguyen, O., Wang, H., Li, A., Muja, N., Henderson, J.E., and Nazhat, S.N. (2010). Reduced hydraulic permeability of three-dimensional collagen scaffolds attenuates gel contraction and promotes the growth and differentiation of mesenchymal stem cells. Acta Biomater. *6*, 3978–3987. https://doi.org/10.1016/j.actbio.2010.04.028.

STAR★METHODS

KEY RESOURCES TABLE

REAGENT or RESOURCE	SOURCE	IDENTIFIER
Antibodies		
alpha-actinin	Sigma-Aldrich	Cat# A7811
Ki-67	Invitrogen	Cat# PIPA519462
Cardiac troponin T (cTnT)	Abcam	Cat# ab8295
von Willebrand Factor (vWF)	Proteintech	Cat# 27186-1-AP
Alexa Fluor 488	Invitrogen	Cat# A-21206
Alexa Fluor 555	Invitrogen	Cat# A-21422
Alexa Fluor 594	Invitrogen	Cat# A-21203
Alexa Fluor 488	Abcam	Cat# ab150169
Green Fluorescent Protein (GFP)	Aves Labs	Cat# GFP-1020
DAPI	Invitrogen	Cat# D1306
Isolectin GS-IB4, Alexa 488 conjugate	Invitrogen	Cat# I21411
Wheat germ agglutinin (WGA) conjugate	Biotium	Cat# 29024-1
Chemicals, peptides, and recombinant proteins		
2-Hydroxy-4'-(2-hydroxyethoxy)-2-methylpropiophenone	Sigma-Aldrich	Cat# 410896
Porcine gelatin	Sigma-Aldrich	Cat# G2500-1KG
Fibrinogen	Sigma-Aldrich	Cat# F8630
Follistatin-like protein 1	Aviscera	Cat# 00347-02-100
Pluronic F-127	Sigma-Aldrich	Cat# P2443-250G
Thrombin	Sigma-Aldrich	Cat# T4648
Citrate buffer	Sigma-Aldrich	Cat# C9999
Critical commercial assays		
alamarBlue Assay	BIO-RAD	Cat# BUF012B
Human Angiogenesis Array Q3	RayBiotech	Cat# QAH-ANG-3-2
Trichrome Stain Kit	Abcam	Cat# ab150686
Experimental models: Cell lines		
GFP-HUVEC	ATCC	PCS-100-013
Experimental models: Organisms/strains		
Rat: Hsd:RH-Foxn1-rnu	Envigo	Cat# 005
Software and algorithms		
Fusion 360	Autodesk	
ImageJ	National Institutes of Health	
GraphPad Prism 10.2.3	GraphPad	

EXPERIMENTAL MODEL AND STUDY PARTICIPANT DETAILS

HUVEC culture

All GFP-HUVEC (ATCC) was cultured in endothelial medium (LL-0003; LIFELINE) on tissue culture flasks and passaged every four to five days with 0.05% Trypsin-EDTA (25-300-054; Gibco). All cells and cell-embedded constructs were maintained at 37°C and 5% CO_2.

Bioink preparation

The GelMA bioink was synthesized as described previously.[54,55,84] A stock solution of 20% (w/v) GelMA with 1% (w/v) Irgacure photoinitiator (410896; Sigma-Aldrich) was used to create a composite bioink. The final GelMA/gelatin/fibrinogen bioink solution was prepared by mixing

each component to the final concentrations of 6% (w/v) GelMA, 5% (w/v) gelatin, and 1% (w/v) fibrinogen (F8630; Sigma-Aldrich). FSTL1 (00347-02-100; Aviscera) was added to the composite bioink at 5 μg/mL to create FSTL1-loaded cardiac patches. GFP-HUVECs were encapsulated in the composite bioink at 10M cells/mL before printing to create a cellular bioink. A sacrificial Pluronic bioink was prepared by mixing Pluronic F-127 (P2443-250G; Sigma-Aldrich) in PBS at 38% (w/v).[84]

Design and biofabrication of cardiac patch constructs

A vascular cardiac patch was designed with computer-aided design (CAD) software (Fusion 360, Autodesk). A disc-shaped patch design (10 mm × 2 mm) with a bifurcating vasculature (1-2-1 vessel tree consisting of 1.4 mm and 1 mm diameter channels) was created. A PDMS mold with the geometry of the patch was used as a fabrication platform in which the patches were manufactured by alternating casting of cellular composite bioink and bioprinting of a sacrificial vascular layer. First, a layer of cellular bioink was cast by pipetting the solution directly into the PDMS mold. Subsequently, a bifurcating vascular pattern was imprinted onto the layer of cellular bioink to pre-form the vasculature. Next, a sacrificial Pluronic ink was used to bioprint the vascular tree layer using an extrusion bioprinter (BioX; CELLINK). Finally, another layer of cellular composite bioink was cast on top of the vascular layer to create a vascular cardiac patch. The fabricated cardiac patch was crosslinked at 2.5 mW/cm^2 for 90s on each side. After crosslinking, the construct was transferred to HUVEC media with 5 U thrombin/mL (T4648; Sigma-Aldrich) overnight to ensure the conversion of fibrinogen to fibrin as well as dissolving of the sacrificial Pluronic to ensure formation of a patent vascular network.

Endothelialization and *in vitro* culture of patch constructs

Channels of the fabricated patch constructs were manually seeded with GFP-HUVECs to endothelialize the lumen of the prefabricated vasculature. On day 1 after patch fabrication, GFP-HUVECs were collected at 8M cells/mL and injected into the empty channels. The seeded constructs were rotated every 15 min for 1 h to ensure uniform attachment of cells. This seeding process was repeated on day 2 with a 180° flipping of constructs. Upon completion of GFP-HUVEC seeding, scaffolds were maintained in static culture for 7 days. Next, the cellular scaffolds were either transferred to perfusion culture or kept in static culture for another 7 days. Dynamic culture of patch constructs was performed by connecting the inlet and outlet of the patch vasculature to the peristaltic pump flow. For this purpose, the patch constructs were inserted into a custom-printed housing, and the inlet of the vasculature was connected to the pump tubing through a needle connector (20G). The outlet of the vasculature was aligned with the exit flow tubing (no needle connector), which was connected to a media reservoir. The flow rate of perfusion culture was set at 200 μL/min. On day 14 of *in vitro* culture, patches were harvested from static or perfusion culture for further analysis.

Creating the rat model of MI – Application of cardiac patch

All studies were performed in accordance with the Guide for the Care and Use of Laboratory Animals and were approved by the Emory Institutional Animal Care and Use Committee. Cardiac patches were studied in athymic nude rats. Male 6-7-week-old Hsd:RH-Foxn1-rnu rats were purchased from Envigo. All animals were randomly allocated to experimental groups. Following our established protocols,[5,7] a left thoracotomy was conducted, and permanent left anterior descending artery (LAD) ligation was performed by placing a 5-0 silk suture ∼2 mm below the left atrium. Ligation was optically confirmed when the LV muscle tissue turned into a pale color. Immediately after MI, the engineered patch was grafted onto the injured myocardium by suturing with one 7-0 silk suture on the periphery of the patch. Study group included the sham control (underwent the left thoracotomy, without MI), MI-only (no treatment), and MI treated with patch or patch + FSTL1. A minimum number of n = 4 was used in each study group.

METHOD DETAILS

Structural fidelity and stability assessment of patch constructs

The structural fidelity of patch constructs was assessed by comparing the geometric dimensions of the CAD model to those of fabricated scaffolds. Cellular constructs were manufactured as described above, and acellular patches were prepared without mixing GFP-HUVECs with the bioink. The diameter and channel sizes were measured using a stereo microscope (SZX7; Olympus). Patch dimensions at day 0 and day 14 were analyzed to assess the structural stability of constructs.

Micromechanical characterization of patch constructs

Microindentation was performed as previously described[33,56,85,86] to characterize mechanical properties of the cardiac patches. Briefly, a microindentation tester (Mach-1; Biomomentum) with a 300 μm spherical probe was used to generate a load-displacement curve. The reduced elastic modulus (E_r) was derived from the unloading curves using the following formula[87]:

$$E_r = \frac{\sqrt{\pi}}{2\beta} \frac{S}{\sqrt{A(h_c)}}$$ (Equation 1)

where β is a constant and equals 1, $A(h_c)$ is projected contact area at the contact depth of h_c. It can be obtained from the following equation:

$$A(h_c) = 2\pi R h_c - \pi h_c^2$$ (Equation 2)

where

$$h_c = h_{max} - \varepsilon \frac{P_{max}}{S} \qquad \text{(Equation 3)}$$

where h_{max} and P_{max} are the peak unloading displacement and unloading force, respectively, and ε is a constant with a value of 0.75 for a spherical indenter.[88]

The elastic modulus, E, can be calculated using the following equation[87]:

$$\frac{1}{E_r} = \frac{(1 - v^2)}{E} + \frac{1 - v_i^2}{E_i} \qquad \text{(Equation 4)}$$

where v is the Poisson's ratio of tested material with a value of 0.5, and v_i is 0.5 for the indenter tip material. E_i represents the elastic modulus of the probe, with a value of 2 GPa.

Ultrastructural analysis – Pore size measurement

Pore diameter of fabricated 3D scaffolds were quantified using scanning electron microscopy (SEM). Patch constructs were fixed in 10% neutral buffered formalin to preserve their morphology. After fixing, samples were washed in deionizied (DI) water, frozen at −80°C, and lyophilized. The freeze-dried samples were examined using an SEM microscope (Axia ChemiSEM; Thermo Scientific). Pore sizes were quantified by measuring the diameters of the imaged pores and plotting histograms as described before.[89–91]

AlamarBlue metabolic activity assay

Metabolic activity of HUVECs in patches was assessed using the AlamarBlue® metabolic activity assay (BUF012B; BIO-RAD) according to the manufacturer's manual.[66,89] Briefly, cellular constructs were exposed to 10% AlamarBlue reagent (v/v) in EC media for 4 h at 37°C and 5% CO_2. Optical density of each supernatant was measured at 550 nm and 600 nm to quantify the metabolic activity as a measure of cell viability and growth.

Immunofluorescent staining of *in vitro* patch constructs

In vitro cultured cellular patches were fixed at 10% natural buffered formalin before immunofluorescent staining. The patches were sectioned at 200 µm thickness perpendicular to the channels, permeabilized, and blocked with 0.25% (v/v) Triton X-100 and 5% donkey serum for 45 min at room temperature. Primary staining was conducted in 5% donkey serum mixed with GFP primary antibody (GFP-1020; Aves Labs) at 1:500 by incubating at 4°C overnight. Secondary staining was performed by incubating sections in secondary antibody (Alexa 488, ab150169; Abcam, 1:500 dilution) at room temperature for 2 h, covered from the light. WGA conjugate antibody (29024-1; Biotium) staining was performed along with secondary antibody staining. Nuclei were stained with DAPI at 1:1000 for 15 min at room temperature. Leica Stellaris 8 confocal microscope was used to image the sections.

Angiogenesis microarray analysis

To analyze the cytokine release profile associated with angiogenesis in culture, a human angiogenesis microarray (QAH-ANG-3-2; RayBiotech) was used according to the manufacturer's protocol.[56] The supernatants of static and perfusion culture media were snap-frozen and stored at −80°C until the assay was performed. The primary incubation with the supernatants was carried overnight at 4°C to ensure sufficient binding of the target cytokines and the antibody array. The secondary incubation with fluorophore-conjugated antibodies was also conducted overnight at 4°C to maximize the signal to noise ratio. The antibody signal was visualized with a microarray scanner (Innoscan 1100AL; Innopsys) and quantified using the data analysis template provided by the manufacturer.

Echocardiography

Cardiac function of rats was monitored at baseline (day 0), and 2 and 4 weeks after patch implantation. Echocardiography was performed on rats using Vevo 3100 (FIJIFILM VisualSonics, Toronto, Canada). The rats were sedated with 2% isoflurane and placed on a heated platform in supine position. Short-axis M-mode images were recorded at mid-LV where papillary muscles were detected. Functional and structural parameters of the heart, including ejection fraction (EF%), fractional shortening (FS%), LV diameters, and LV wall thicknesses were calculated from the short-axis view echocardiogram.

Histology and immunohistochemical analysis of patch-treated hearts

Histological analysis was used to evaluate the hearts at the tissue and cellular level. Masson's trichrome staining was performed according to the manufacturer's protocol for paraffin embedded samples. Hearts were harvested and fixed in formalin, processed, and embedded in paraffin. The embedded hearts were sectioned at 10 µm thickness, unless noted otherwise. The fibrosis level was measured from histological analyses, by quantifying the surface area of infarcted myocardial tissue (blue staining) within the LV. Immunohistochemical staining was performed to assess cellular response to the cardiac patch treatment. Paraffin embedded heart sections were first deparaffinized in xylenes and rehydrated with serial dilutions of ethanol. The sections were then permeabilized with 0.25% Triton X-100 for 15 min and antigen retrieved in

pH 6 citrate antigen retriever buffer (C9999; Sigma-Aldrich). The tissue sections were blocked in 5% donkey serum for 1 h at room temperature. Primary staining was performed by incubating the tissue sections in primary antibody solutions (α-actinin (A7811; Sigma-Aldrich) at 1:250, Ki-67 (PIPA519462; Invitrogen) at 1:200, cTnT (ab8295, Abcam) at 1:250, vWF (27186-1-AP; Proteintech) at 1:200 dilutions in 5% donkey serum at 4°C overnight. Secondary antibodies (Alexa Fluor 488, Alexa Fluor 555, and Alexa Fluor 594 from Invitrogen) and conjugated antibodies (IB4, 488 conjugate (I21411; Invitrogen)) were used at 1:500 dilution in 5% donkey serum for 2 h at room temperature in dark. CM growth and angiogenesis were evaluated by counting the number of proliferating CM as well as the cross-sectional area of vessels normalized by the surface area.

QUANTIFICATION AND STATISTICAL ANALYSIS

All experimental data were processed and presented using means ± standard error of means (SEM). Statistical significance was determined by one-way or two-way analysis of variance (ANOVA) with Tukey's test via GraphPad Prism 10.2.3. The statistical tests used for each experiment are indicated in the figure legends. The p-value <0.05 was considered statistically significant in the entire study (*: $p < 0.05$, **: $p < 0.01$, ***: $p < 0.005$, and ****: $p < 0.001$). All data are represented as mean ± SEM.